Upward Pipe-Soil Interaction for Shallowly Buried Pipelines in Dense Sand

Kshama Roy[1], Bipul Hawlader[2*], Shawn Kenny[3] and Ian Moore[4]

[1]Pipeline Stress Specialist, Northern Crescent Inc., 816 7 Ave SW, Calgary, Alberta T2P 1A1, Canada; formerly PhD Candidate, Department of Civil Engineering, Faculty of Engineering and Applied Science, Memorial University of Newfoundland, St. John's, Newfoundland and Labrador A1B 3X5, Canada

[2]**Corresponding Author:** Professor and Research Chair in Seafloor Mechanics, Department of Civil Engineering, Faculty of Engineering and Applied Science, Memorial University of Newfoundland, St. John's, Newfoundland and Labrador A1B 3X5, Canada
Tel: +1 (709) 864-8945 Fax: +1 (709) 864-4042 E-mail: bipul@mun.ca

[3]Associate Professor, Department of Civil and Environmental Engineering, Faculty of Engineering and Design, Carleton University, 1125 Colonel By Drive, Ottawa, ON, K1S 5B6

[4]Professor and Canada Research Chair in Infrastructure Engineering, GeoEngineering Centre at Queen's – RMC, Queen's University, Kingston, ON, K7L 4V1

Number of Figures: 9

Number of table: 2

KEYWORDS: pipeline, Mohr–Coulomb model, finite element analyses, dense sand, upward movement

Abstract: The uplift resistance is a key parameter against upheaval buckling in the design of a buried pipeline. The mobilization of uplift resistance in dense sand is investigated in the present study based on finite element (FE) analysis. The pre-peak hardening, post-peak softening, and density and confining pressure dependent soil behaviour are implemented in FE analysis. The uplift resistance mobilizes with progressive formation of shear bands. The vertical inclination of the shear band is approximately equal to the maximum dilation angle at the peak and then decreases with upward displacement. The force–displacement curves can be divided into three segments: pre-peak, quick post-peak softening, and gradual reduction of resistance at large displacements. Simplified equations are proposed for mobilization of uplift resistance. The results of FE analysis, simplified equations and model tests are compared. The importance of post-peak degradation of uplift resistance to upheaval buckling is discussed.

Introduction

Buried pipelines used for transporting oil usually operate at high temperature and pressure. Temperature induced expansion, together with vertical out-of-straightness, might cause global upheaval buckling (UHB). Field evidence suggests that significantly large vertical upward displacement could occur in the buckled section and, in the worst cases, it might protrude above the ground surface (Palmer et al. 2003). For example, Aynbinder and Kamershtein (1982) showed that a ~70 m section of a buried pipeline displaced vertically up to a maximum distance of ~4.2 m above the ground surface. Sufficient restraint from the soil above the pipeline could prevent excessive displacement and upheaval buckling. As burial is one of the main sources of pipeline installation cost, proper estimation of soil resistance is necessary to select the burial depth—typically expressed as the embedment ratio ($\widetilde{H}$ = H/D), where D is the diameter and H is the depth of the center of the pipe. Pipelines embedded at $1 \leq \widetilde{H} \leq 4$ in dense sand are the focus of the present study, although it is understood that in some special scenarios $\widetilde{H}$ could be outside this range, for example, for surface laid offshore pipelines in deep water (Dutta et al. 2015) or the pipelines in ice gouging areas (Pike and Kenny 2016).

During installation of offshore pipelines in sand, ploughs deposit backfill soil in a loose to medium dense state (Cathie et al. 2005); however, it could be subsequently densified due to environmental loading. For example, Clukey et al. (1989) showed that the sandy backfill of a test pipe section densified from relative density (D_r) less than ~57% to ~85–90% in 5 months, which has been attributed to wave action at the test site in the Gulf of Mexico. The uplift resistance offered by soil (F_v) depends on upward displacement (v) and generally comprises three components: (i) the submerged weight of soil being lifted (W_s); (ii) the vertical component of shearing resistance offered by the soil (S_v); and (iii) suction under the pipe (F_{suc}). The component F_{suc} could be neglected for a drained loading condition at low uplift velocities (Bransby and Ireland 2009; Wang et al. 2010). The force–displacement behaviour is generally expressed in normalized form using $N_v = F_v/\gamma HD$ and $\tilde{v} = v/D$, where γ is the effective unit weight of soil, which is the dry unit weight in physical model tests and FE modelling of uplift behaviour presented in this study. Physical experiments show that N_v increases with $\widetilde{H}$ and D_r (Trautmann 1983; Bransby et al. 2002; Chin et al. 2006; Cheuk et al. 2008). A close examination of physical model test results in dense sand at $\widetilde{H} \leq 4$ shows that N_v increases quickly with $\tilde{v}$ and reaches the peak (N_{vp}) at $\tilde{v} \sim 0.01$–0.05. A quick reduction of N_v occurs after the peak followed by gradual reduction of N_v at large $\tilde{v}$. The ALA guideline for design (ALA 2005) does not explicitly consider the post-peak reduction of N_v and the maximum $N_v = \phi\widetilde{H}/44$ is recommended, where ϕ' is a representative angle of internal friction (in degree). However, DNV (2007) recognized the post-peak reduction of N_v and recommended a N_v–$\tilde{v}$ relation using four linear line segments in which N_v reduces linearly from the peak to a residual value with $\tilde{v}$ and then remains constant.

The load–displacement curves obtained from model tests evolve from complex deformation mechanisms and the stress–strain behaviour of soil above the pipe. To understand these mechanisms, the particle image velocimetry (PIV) technique (White et al. 2003) has been used in recent model tests (Cheuk et al. 2008; White et al. 2008; Thusyanthan et al. 2010; Wang et al. 2010). When the peak uplift resistance mobilizes in medium to dense sand, two inclined symmetric slip planes form in the backfill soil, starting from the springline of the pipe (White et al. 2008). Although the slip planes slightly curve outwards, their inclination to the vertical (θ) is approximately equal to the peak dilation angle (ψ_p). The vertical inclination of slip planes decrease with $\tilde{v}$, and they become almost vertical at large $\tilde{v}$. A model test conducted by Huang et al. (2015) shows that θ gradually increases in the pre-peak, reaches ~ψ_p at the peak N_v and then decreases in the post-peak zone.

PIV data provide very useful information on soil deformation patterns; however, the progressive formation of shear bands in dense sand due to strain-softening can be better explained by using numerical modelling techniques. More specifically, the post-peak reduction of N_v, as recommended in DNV (2007), could be examined/revised, implementing an appropriate soil constitutive model that can simulate the strain-softening behaviour of dense sand, change in θ and cover depth with $\tilde{v}$. The pre-peak hardening, post-peak softening, relative density and confining pressure (p') dependent ϕ' and ψ are the common features of the stress–strain behaviour of dense sand. In addition, the mode of shearing (triaxial (TX) or plane strain (PS)) significantly influences ϕ' and ψ. All of these features of the stress–strain behaviour of dense sand have not been considered in the available guidelines or FE analyses. A large number of FE analyses has been conducted using the Mohr–Coulomb (MC) model with constant ϕ' and ψ and therefore cannot model post-peak reduction of N_v, except for the reduction due to change in cover depth (Yimsiri et al. 2004; Farhadi and Wong 2014). Yimsiri et al. (2004) also used an advanced soil model (Nor-Sand); however, they could not simulate the significant reduction of N_v, as observed in model tests. Chakraborty and Kumar (2014) used the MC model for the lower bound FE limit analysis. Jung et al. (2013) incorporated linear reduction of ϕ' and ψ after the peak with plastic shear strain; however, they did not consider the pre-peak hardening. Jung et al. (2013) also showed the importance of using PS strength parameters for pipe–soil interaction.

In addition to physical and numerical modelling, limit equilibrium and plasticity solutions have also been proposed to calculate the normalized peak uplift resistance, N_{vp} (White et al. 2008; Merifield et al. 2001). As soil in these solutions is constrained to satisfy normality (i.e. $\theta = \psi = \phi'$), the plasticity solutions give a more non-conservative uplift resistance than the limit equilibrium solutions with $\theta = \psi_p$ ($< \phi'$) (White et al. 2008).

The objective of the present study is to conduct FE analysis to examine uplift behaviour of shallow buried pipelines in dense sand ($\widetilde{H} \leq 4$). An advanced soil constitutive model is adopted in FE analysis to simulate not only the peak but also the post-peak uplift resistance. The FE model is validated against a physical model test and numerical results. A set of empirical equations is proposed to develop the uplift resistance versus displacement curve, including the post-peak degradation at large displacements. Finally, conducting FE analysis for structural response, the importance of post-peak uplift resistance on upheaval buckling is shown.

Modelling of Soil

The Mohr−Coulomb (MC) and a modified Mohr−Coulomb (MMC) models are used in this study. In the MMC model, ϕ' and ψ vary with relative density (D_r), mean effective stress (p') and accumulated plastic shear strain (γ^p). The details of the MMC model, including the required parameters and calibration against laboratory test data, are available in Roy et al. (2016). The mathematical equations are listed in Table 1.

The novel aspects of the MMC model, compared to the models of similar type used in pipe–soil interaction analysis (e.g. Jung et al. 2013; Pike 2016), is that the nonlinear variation of pre- and post-peak ϕ' and ψ with γ^p are defined with smooth transitions at the peak and critical state. This has a considerable influence on the uplift force–displacement response of a buried pipeline because the size of the failure wedge and soil resistance to upward movement of the pipe depend on ϕ' and ψ.

Finite Element Modelling

Two-dimensional FE analyses in plane strain condition are performed using Abaqus/Explicit FE software (Dassault Systèmes 2010). Figure 1 shows the typical FE mesh at the start of uplifting. Taking advantage of symmetry, only half of the domain is modelled. A dense mesh is used near the pipe (Zone-A), where considerable soil deformation is expected. To avoid mesh distortion issues at large displacements, an adaptive remeshing option in Abaqus is adopted in Zone-A, which creates a new smooth mesh at a regular interval to maintain a good aspect ratio of the elements. In Abaqus/Explicit, the remeshing is performed using the arbitrary Lagrangian-Eulerian method, without changing the number of elements, nodes and connectivities. The bottom of the FE domain is restrained from horizontal and vertical movement, while all the vertical faces are restrained from any lateral movement. Mesh sensitivity analyses are performed to select an optimal mesh (Roy 2017).

Four-node bilinear plane strain quadrilateral elements (CPE4R in Abaqus) are used for modelling the soil. The pipe is modelled as a rigid body. The bottom and left boundaries are placed at a sufficiently large distance from the pipe to avoid boundary effects on uplift behaviour.

The pipe–soil interface is modelled by defining the interface friction coefficient (μ) as $\mu = \tan(\phi_\mu)$, where ϕ_μ is the pipe–soil interface friction angle. ϕ_μ depends on pipe surface roughness and ϕ' of the soil around the pipe. With loading, the soil elements around the pipe experience high shear strains that cause a reduction of ϕ'. Therefore, assuming a looser soil condition, $\mu = 0.32$ is used. Note that μ has a little influence on the uplift resistance and $\mu = 0.2$–0.6 gives less than 2% variation in the peak resistance. The numerical analysis is conducted in two steps. In the first step, geostatic stress is applied under $K_0 = 0.5$, where K_0 is the at-rest earth pressure coefficient. The value of K_0 does not significantly affect the uplift resistance in FE analysis (Jung et al. 2013). In the second step, the pipe is displaced up by specifying a displacement boundary condition at the reference point (center of the pipe).

The MMC model is implemented in Abaqus by developing a user subroutine VUSDFLD written in FORTRAN. The stress and strain components are called in the subroutine in each time increment.

The mean effective stress (p') is calculated from the three principal stresses. The strain components are transferred to the principal strain components and stored as state variables. The plastic strain increment ($\Delta\gamma^p$) in each time increment is calculated as $\Delta\gamma^p = (\Delta\varepsilon_1^p - \Delta\varepsilon_3^p)$, where $\Delta\varepsilon_1^p$ and $\Delta\varepsilon_3^p$ are the major and minor principal plastic strain components, respectively. The value of γ^p is calculated as the sum of $\Delta\gamma^p$ over the period of analysis. In the subroutine, γ^p and p' are defined as two field variables. The mobilized ϕ' and ψ are defined in the input file as a function of γ^p and p' in tabular form, using the equations in Table 1. During the analysis, the program accesses the subroutine and updates the values of ϕ' and ψ with field variables. Note that, although I_D is not updated in each time increment, the volumetric change in soil elements due to shearing and its effects on ϕ' and ψ are captured in the MMC model.

Model Verification

FE simulation is first performed for a physical model test conducted by Cheuk et al. (2005, 2008) at the University of Cambridge and is called the CD (coarse dense sand) test. A 100 mm diameter model pipe section embedded at $\widetilde{H}$ = 3 in dry Leighton Buzzard silica sand was pulled up slowly at 10 mm/h to capture soil deformation using two digital cameras. However, in FE modelling the pipe is pulled at ~10 mm/s by maintaining quasi-static simulation condition.

Direct shear tests show that Leighton Buzzard (LB) silica sands has ϕ'_c of 32° (Cheuk et al. 2008). As ϕ'_c in PS condition could be ~2°–4° higher than in direct shear conditions (Lings and Dietz 2004), $\phi'_c = 35°$ is used, which is ~ 3° higher than DS tests results reported by Cheuk et al. (2008). For quartz and siliceous sands, $Q \sim 10 \pm 1$ (Randolph et al. 2004; Bolton 1986). Although the values are within this range, Chakraborty and Salgado (2010) showed a trend of increasing Q with initial confining pressure (< 196 kPa). In this study, Q = 10 and R = 1 is used. Bolton (1986) suggested A_ψ = 5 and k_ψ = 0.8 for PS condition based on analysis of a large number of laboratory tests results on different sands. Roy et al. (2016) calibrated the present MMC model against laboratory test results on

Cornell filter (CF) sand and obtained the values of C_1, C_2 and m to model the variation of ϕ' and ψ with γ^p, and then conducted FE simulation of physical model tests of Trautmann (1983). Cheuk et al. (2008) did not provide any stress–strain curve of LB sand used in physical modelling. Both of these physical model test programs used uniform/poorly graded sand, although the mean particle size (D_{50}) of the coarse fraction of LB sand is larger (D_{50} ~ 2.24 mm) in Cheuk et al. (2008) than that of CF sand (D_{50} ~ 0.5 mm) in Trautmann (1983). However, based on laboratory test results, Cheuk et al. (2008) recognized a minimal influence of particle size on frictional characteristics of LB sands—the peak and critical state friction angles are 52° and 32°, respectively, for a coarse and a fine fraction of LB sand. Furthermore, in Cheuk et al. (2008), the force–displacement curves for the coarse and fine fractions of LB sands are similar, including the peak and post-peak degradation. Therefore, in the present study, the values of C_1, C_2 and m of LB sand are assumed to be the same as CF sand. Table 2 shows the geotechnical parameters used in FE analyses. Figure 1(b) shows the typical variation of ϕ' and ψ with plastic shear strain.

Force–displacement behaviour

Figure 2 shows the FE simulated force–displacement curves for $\widetilde{H}$ = 3, on which the points of interest for further explanation are labeled A–E for the MMC and A′–E′ for the MC model. Note that, adaptive remeshing could not maintain a high quality mesh at a very large pipe displacement. Therefore, the force–displacement curves only up to $\tilde{v}$ = 1.0 are presented in this study. For MMC, N_v increases quickly and reaches the peak at $\tilde{v}$ ~ 0.03 and then quickly decreases to point C, primarily due to the strain-softening behaviour of soil. After a slight increase between points C and D, N_v decreases again at a slower rate than in the segment AC. In the present study, the segment AC of the N_v–$\tilde{v}$ curve is termed the "softening segment" and the segment after point C is called the "large deformation segment." The values of N_v at the peak and after softening (i.e. points A and C) are defined as N_{vp} (= $F_{vp}/\gamma HD$) and N_{vs} (= $F_{vs}/\gamma HD$), respectively, where F_{vp} and F_{vs} are the peak and after softening uplift resistances, respectively. The dimensionless uplift displacement, $\tilde{v}$, required to mobilize N_{vp} and N_{vs}, are defined as $\tilde{v}_p$ and $\tilde{v}_s$, respectively.

The mobilization of N_v shown in Fig. 2 could be explained from progressive development of shear bands, the zones of localized plastic shear strain, $\gamma^p = \int_0^t \sqrt{\frac{3}{2}(\dot{\epsilon}_{ij}^p \dot{\epsilon}_{ij}^p dt)}$, where $\dot{\epsilon}_{ij}^p$ is the plastic deviatoric strain rate tensor (Figs. 3(a)–3(e)). At N_{vp}, plastic shear strain mainly develops locally in an inclined shear band originating from the springline of the pipe; however, the shear band does not reach the ground surface for formation of a complete slip mechanism (Fig. 3(a)). The inclination of the shear band to the vertical (θ) is obtained by drawing a line from the pipe surface through the highly concentrated γ^p zone. White et al. (2008) suggested that $\theta \sim \psi_p$ when the peak resistance is mobilized. As ψ_p varies with p' (see Table 1), they calculated a single representative value of the peak dilation angle (ψ_p^R) using the in-situ p' at the springline of the pipe ($(1+2K_0)\gamma H/3$). For the geotechnical parameters listed in Table 2, ψ_p^R = 25°, which is approximately the same as θ obtained from the present FE analysis (Fig. 3(a)). The complete slip mechanism develops at $\tilde{v} > \tilde{v}_p$ when a considerable post-peak degradation of N_v occurs (Fig. 3(b)). Similar types of curved failure planes shown in Figs. 3(b)–3(e) were also observed in model tests (Stone and Newson 2006; Cheuk et al. 2008; Huang et al. 2015). The formation of complete slip planes after $\tilde{v}_p$ can be attributed from noticeable vertical displacement of the ground surface after N_{vp} in model tests (Dickin 1994; Bransby et al. 2002; Huang et al. 2015).

It is worth noting that, although it is a different type of loading, because of progressive development of shear bands, the attainment of peak load before the formation of a complete failure mechanism was also found in model tests and numerical modelling for footing in dense sand (Tatsuoka et al. 1991; Aiban and Znidarčić 1995; Loukidis and Salgado 2011). Note, however, that in the simplified limit equilibrium method (LEM), a complete slip mechanism is assumed to calculate the peak load irrespective of burial depth; for example, White et al. (2008) used the LEM to fit test data for $\widetilde{H} < 8.0$.

The slight increases in N_v in the segment CD in Fig. 2 can be explained using γ^p plots in Figs. 3(a)–3(d). In the segment ABC of the N_v–$\tilde{v}$ curve, the shear resistance (τ_f) gradually reduces along the inclined shear band that was formed during initial upward displacement (e.g. Figs. 3(a)–3(c)). However, the location of the shear band shifts considerably to the right at $\tilde{v}$ ~ 0.18–0.4. As the new shear bands form through the soil where τ_f has not been reduced by softening, N_v increases slightly in the segment CD. After point D, the location of the shear band does not change significantly with $\tilde{v}$ (θ remains ~ 8°). Therefore, the gradual decreases of N_v with $\tilde{v}$ after point D is due to strain-softening in the shear band and the reduction of soil cover depth.

Figure 2 also shows that an FE simulated N_v–$\tilde{v}$ curve with the MMC model compares well with the model test results of Cheuk et al. (2008). A slight increase in N_v after a quick post-peak reduction is also observed in model tests at intermediate depth of embedment, as the one shown in Fig. 2 and also in other studies (Bransby et al. 2002; Stone and Newson 2006; Chin et al. 2006; Cheuk et al. 2008; Saboya et al. 2012; Eiksund et al. 2013; Huang et al. 2015). However, it does not happen at shallow burial depths. A similar trend is also observed in model tests for the bearing capacity of footing in sand, which has been attributed to progressive formation of slip planes (Aiban and Znidarčić 1995).

The inclination of the shear band gradually reduces with $\tilde{v}$, and at $\tilde{v} = 0.32$, θ ~ 8° (Fig. 3(c)). However, θ does not reduce further at $\tilde{v} > 0.32$ (Figs. 3(c)–3(e)). As discussed later, in the limit analysis $\theta = 0$ is assumed at large $\tilde{v}$; however, the present FE analysis shows that the shear band does not become completely vertical even at large $\tilde{v}$ (e.g. $\tilde{v} = 0.5$). Because of change in mobilized ϕ' and ψ with loading, the failure mechanism changes from an inclined slip plane (Fig. 3(b)) to a flow around mechanism (Fig. 3(e)). See also the velocity vectors in the inset of Fig. 2. Based on PIV results, similar failure mechanisms have been reported from physical experiments (Bransby et al. 2002; Cheuk et al. 2008).

Limitations of Mohr–Coulomb model

To show the advantages of the MMC model, FE simulation is also performed with the MC model. Based on Cheuk et al. (2005, 2008) laboratory test results $\phi' = 52°$ and $\psi = 25°$ are used for the MC model. Although it is not explicitly mentioned in the design guidelines, equivalent values for these two parameters should be carefully selected, as they vary with γ^p. In general, the equivalent values of ϕ' and ψ should be smaller than the peak and higher than the critical state values. A number of previous studies simulated pipe–soil interaction using constant equivalent values for the MC model (e.g. Yimsiri et al. 2004). Note that an equivalent ϕ' has also been recommended for other geotechnical problems in dense sand, for example, the bearing capacity of shallow foundations (Loukidis and Salgado 2011) and the lateral capacity of pile foundations (API 1987).

Figure 2 shows that the MC model calculates slightly higher N_{vp} than the MMC model. This difference will be reduced if lower equivalent values of ϕ' and ψ are considered. However, the key observation is that N_v decreases almost linearly with $\tilde{v}$ after the peak for the MC model, which is very different from the simulation with the MMC model and physical model test results. In order to explain this force–displacement behaviour, γ^p at five $\tilde{v}$ is plotted in Figs. 3(f)–3(j). The inclination of the shear band (θ) remains almost constant (~ 25°) during the whole process of upward displacement of the pipe. The linear post-peak reduction of N_v with the MC model is due to the reduction of cover depth with $\tilde{v}$.

In summary, the post-peak reduction of N_v with the MMC model for this burial depth occurs due to the combined effects of three factors: (i) decreases in size of the failure wedge, (ii) reduction of shear resistance with γ^p, and (iii) reduction of cover depth. The MC model cannot capture the effects of the former two. However, the proposed MMC model can simulate the effects of all three factors. Moreover, the simulations with the MMC model are similar to physical model test results.

DNV (2007) suggested the following equations to develop the force–displacement curve for dense sand for $2.5 \leq \widetilde{H} \leq 8.5$: $N_{vp} = 1 + f\widetilde{H}$; $N_{vs} = 1 + \alpha_f f\widetilde{H}$; $\tilde{v}_p = (0.5\% \text{ to } 0.8\%)\widetilde{H}$ and $\tilde{v}_s = 3\tilde{v}_p$. The pre-peak behaviour is defined by a bi-linear relation, where the slope changes at (αN_{vp}, $\beta\tilde{v}_p$). Based on DNV (2007) recommendations for dense sand, $f = 0.6$, $\alpha_f = 0.75$, $\tilde{v}_p = 0.008\widetilde{H}$, $\alpha = 0.75$, $\beta = 0.2$; the force–displacement curve is plotted in Fig. 2. Although only one test is simulated, DNV (2007) gives considerably lower N_{vp}, higher N_{vs} and lower $\tilde{v}_s$ than the physical model test and present FE results with the MMC model.

The maximum N_v based on ALA (2005) (= $\phi\widetilde{H}/44$) is shown by two horizontal arrows on the right vertical axis for two ϕ'. Note that ALA (2005) requires a constant equivalent ϕ', and does not consider any post-peak reduction of resistance.

Effect of Burial Depth

Figure 4 shows the load–displacement curves for $\widetilde{H} = 1$–4. FE modelling for $\widetilde{H} > 4$ is available in Roy et al. (2018). Although the simulation is performed for every $\widetilde{H} = 0.5$ interval, only four curves are shown in Fig. 4 for clarity. Three key features of the N_v–$\tilde{v}$ curves are: (i) although N_{vp} (open circles) increase with $\widetilde{H}$, $\tilde{v}_p \sim 0.03$ for the cases analyzed; (ii) $\tilde{v}_s$ increases with $\widetilde{H}$; and (iii) the slope of the curve at large deformation (i.e. after open squares) decreases with $\widetilde{H}$.

A number of studies and design guidelines discussed $\tilde{v}_p$ and N_{vp}, and therefore, a very brief discussion of these two values is provided. In general, $\tilde{v}_p$ decreases with D_r and increases with $\widetilde{H}$ (Trautmann 1983; Dickin 1994; ALA 2005; DNV 2007). Cheuk et al. (2008) found $\tilde{v}_p \sim 0.03$ or $0.01H$ from model tests on dense sands. For the range of soil properties and burial depths considered in the present FE analysis, $\tilde{v}_p$ does not vary significantly with $\widetilde{H}$ between 1 and 4. However, FE simulations show a significant increase in $\tilde{v}_p$ with $\widetilde{H}$ for deep burial conditions (Roy et al. 2018). Figure 5 shows that N_{vp} for the MMC model increases almost linearly with $\widetilde{H}$. Moreover, N_{vp} obtained from the present FE analysis is comparable to available physical model tests and FE results.

The mobilized N_v after a quick post-peak reduction (i.e. N_{vs}), shown by the squares in Fig. 4, increases with $\widetilde{H}$. However, unlike $\tilde{v}_p$, the displacement at N_{vs} (i.e. $\tilde{v}_s$) increases with $\widetilde{H}$.

Proposed Simplified Equations for Uplift Force–Displacement Curve

The solid lines in Fig. 4 show the proposed N_v–$\tilde{v}$ relation for simplified analysis, which is comprised of a bilinear curve up to N_{vs} followed by a slightly nonlinear curve at large displacements. Note that DNV (2007) recommended that N_v remains constant after N_{vs} (cf. Fig. 2). The parameters required to define the proposed N_v–$\tilde{v}$ relation are F_{vp}, v_p, F_{vs} and v_s.

Peak resistance

Depending on slip plane formation, *inclined* and *vertical* slip plane models are commonly used to calculate uplift resistance (Schaminee et al. 1990; White et al. 2008). In the former one, the slip plane forms at an angle θ to the vertical, while $\theta = 0$ in the latter one. Experimental studies show that the vertical slip plane model is primarily applicable to loose sand at medium $\widetilde{H}$ (White et al. 2001; Wang et al. 2010). For dense sand, two symmetrical inclined slip planes form from the springline of the pipe at $\theta \sim \psi_p^R$ (White et al. 2008; Huang et al. 2015).

Based on limit equilibrium method (LEM), the peak uplift resistance (F_{vp}) can be calculated from an inclined slip plane model as the sum of the weight of the lifted soil wedge (W_s) and the vertical component of shearing resistance along the two inclined planes (S_v).

$$F_{vp} = \gamma D^2 \left[\left\{ \widetilde{H} - \left(\frac{\pi}{8}\right) + \widetilde{H}^2 \tan\theta \right\} + F_A \widetilde{H}^2 \right] \quad (1)$$

where

$$F_A = \left(\tan\phi_p' - \tan\theta\right) \left[\frac{1 + K_0}{2} - \frac{(1 - K_0)\cos 2\theta}{2} \right] \quad (2)$$

Equations (1 &2) are derived assuming that, the inclined slip surfaces reach the ground surface when F_{vp} mobilizes, causing global failure of the soil block. The first part of the right hand side of Eq. (1) represents the contribution of W_s while the second part is for S_v.

The lifting of the pipe reduces the cover depth and inclined length of slip planes, although it does not have significant effects on F_{vp} because $\tilde{v}_p$ is very small. However, lifting has a significant effect on F_{vs}, as discussed in the following sections. In order to be consistent in the proposed equations for the peak and post-peak resistances (Eqs. (3) & (4)), the lifting effect is also incorporated in the following revised equation for the peak resistance. In other words, the uplift resistance is calculated based on the current position of the pipe $\left(\widetilde{H} - \tilde{v}_p\right)$.

$$F_{vp} = R\gamma D^2 \left[\left\{\left(\widetilde{H} - \tilde{v}_p\right) - \frac{\pi}{8} + \left(\widetilde{H} - \tilde{v}_p\right)^2 \tan\theta\right\} + F_A\left(\widetilde{H} - \tilde{v}_p\right)^2\right] \quad (3)$$

The reduction factor R is discussed in the following sections.

Effects of shear band formation on peak resistance

Figure 6(a) shows the mobilized ϕ' and formation of slip planes for four embedment ratios. While $\theta \sim \psi_p^R = 25°$ is used to define the soil wedge in the LEM, the slip planes in FE simulations are located on the right side of this line and curve outwards near the ground surface. Therefore, the weight of the lifted soil wedge is less in FE simulations than the LEM, especially for a large $\widetilde{H}$ (e.g. $\widetilde{H}$ = 4). Moreover, although $\phi' = \phi'_p$ is used in the LEM, this is valid only for a small segment of the slip plane (e.g. near the point A in Fig. 6(a) for $\widetilde{H}$ = 3). Below this point, $\phi' < \phi'_p$ because the large plastic shear strain (γ^p) causes strain-softening. Above this point, γ^p is not sufficiently large (i.e. $\gamma^p < \gamma_p^p$) to mobilize ϕ'_p, therefore ϕ' is less than ϕ'_p also in this segment of the slip plane. The ratio between the pre- and post-peak segments of the slip plane increases with embedment ratio.

Overestimation of W_s and ϕ' gives a higher F_{vp} in the LEM (F_{vp_LEM}) than FE simulation (F_{vp_FE}). In order to investigate this effect, FE simulations are performed for a varying embedment ratio ($\widetilde{H}$ = 1–4), diameter (D = 100–500 mm) and relative density of dense sand (D_r = 80–90%). It is found that change in D_r in this range has minimal influence on pipeline response because ϕ'_p and ψ_p remain the same, as I_R = 4.0 at a low mean stress and high relative density (Bolton 1986), although γ_p^p slightly decreases with an increase in D_r (see first four equations in Table 1). Note that the proposed MMC model should not be applicable to loose to medium dense sands, as it cannot capture the volumetric compression due to shear.

Figure 6(b) shows that the reduction factor R (= F_{vp_FE}/F_{vp_LEM}) decreases with an increase in embedment ratio, which is because of overestimation of W_s and ϕ' in the LEM as discussed above. Moreover, R is almost independent of pipe diameter. The overestimation of uplift resistance in LEM is significant at large embedment ratios—for example, the LEM calculates ~ 22% higher peak resistance than FE calculated value for $\widetilde{H}$ = 4.

Uplift resistance after initial softening

Similar to Eq. (3), a simplified equation is proposed for the uplift force after initial softening, F_{vs} (Eq. (4)). At a large displacement, the failure planes reach the ground surface (Fig. 3(c)) and therefore R = 1 is used. As significant strain-softening occurs, ϕ' along the slip planes reduces almost to ϕ'_c. Considerable ground surface heave occurs at this stage (Fig. 3(c)), which increases with pipe displacement and its maximum height above the pipe is smaller than v. At a large v, surface heave occurs over a wider zone than the width of the soil wedge at the ground surface defined by θ (< ψ_p^R) in the LEM. Based on this observation, the additional weight due to surface heave is calculated assuming a trapezoidal soil wedge having slope angle α (≤ ϕ'_c) and height 0.9v, as shown in Fig. 8(b), for simplified equation (Eq. (4)). The base width of the trapezoid is obtained by drawing two slip planes at $\theta = \psi_p^R$. Note that a trapezoidal heave was also observed in physical experiments (Schupp et al. 2006; Wang et al. 2012). The following equation is proposed for F_{vs}.

$$F_{vs} = \gamma D^2 \left[\left\{ \left(\widetilde{H} - \tilde{v}_s\right) - \frac{\pi}{8} + \left(\widetilde{H} - \tilde{v}_s\right)^2 \tan\theta \right\} + \left\{ F_A \left(\widetilde{H} - \tilde{v}_s\right)^2 \right\} \right.$$
$$\left. + 0.9\tilde{v}_s \left\{ 1 + \left(\widetilde{H} - \tilde{v}_s\right) \tan\psi_p^R \right\} \right] \quad (4)$$

As the slip plane does not become completely vertical (Figs. 3(c)–3(e)), $\theta = 8°$ is used to calculate F_{vs} using Eq. (4). Finally, replacing $\tilde{v}_s$ by $\tilde{v}$ in Eq. (4), the uplift resistance at large displacements ($\tilde{v} > \tilde{v}_s$) can be calculated.

Displacement at peak resistance and initial softening

Although it is not noticeable in Fig. 4, a very small increase in $\tilde{v}_p$ with $\widetilde{H}$ is found, which can be approximately represented as $\tilde{v}_p = 0.002\widetilde{H} + 0.025$. However, a considerable increase in $\tilde{v}_s$ with $\widetilde{H}$ is found, which can be expressed as $\tilde{v}_s = 0.0035\widetilde{H} + 0.1$. However, one should not extrapolate these empirical equations outside this range of $\widetilde{H}$ (= 1–4) simulated in this study because the failure mechanisms could be very different. For example, the pipeline will be partially embedded if $\widetilde{H} < 0.5$. On the other hand, flow around mechanisms govern the response for large $\widetilde{H}$.

FE results show that the ratio $\tilde{v}_s/\tilde{v}_p$ is greater than 3, as recommended in DNV (2007), especially for a large $\widetilde{H}$. One potential reason is that, at a large $\widetilde{H}$, the formation of the inclined shear band continues even after the peak until it reaches the ground surface, which requires some additional upward displacement of the pipe (Figs. 3(a) & 3(b)).

Comparison between simplified equations and FE results

Figure 4 shows that the proposed equations can model the force–displacement behaviour obtained from FE simulations. In this figure, the solid lines are drawn by calculating F_{vp} and F_{vs} using Eqs. (3) and (4), respectively, and then dividing the values by γHD. The value of R in Eq. (3) is obtained from Fig. 6(b).

Figure 7(a) shows that Eq. (3) without the reduction factor (i.e. R = 1) calculates higher peak resistance than FE result, and the difference increases with $\widetilde{H}$ because of overestimation of W_s and mobilized friction angle. When R (= 0.8–0.95) is adopted, as in Fig. 6(b), the calculated peak resistance using Eq. (3) compares well with FE results, which is also comparable to ALA (2005) but higher than DNV (2007) (cf. Fig. 5). When the effects of surface heave are considered, the calculated resistance after initial softening using Eq. (4) (i.e. squares in Fig. 4) also agrees well with FE results.

The contributions of W_s and S_v on N_{vp} and N_{vs} are evaluated using Eqs. (3), and (4) and are shown in Fig. 7(b). Note that the sum of the first and third part in Eq. (4) is considered as W_s. The vertical resistance offered by W_s is higher than that of S_v. Comparing the contribution of W_s on N_{vp} (where $\theta \sim \psi_p^R$ = 25°) and on N_{vs} (where θ ~ 8°), it can be concluded that θ has a significant effect on uplift resistance. Similarly, the contribution of S_v on N_v increases significantly with θ, which depends on soil property and more specifically on dilation angle. Therefore, an appropriate soil constitutive model, like the one used in the present study, is required for modelling uplift resistance.

The performance of the proposed simplified equations is explained further by plotting F_v against $(\tilde{v} - \widetilde{H})$ as in Fig. 8(a). The calculated N_{vs} using Eq. (4) without surface heave is ~10% smaller than N_{vs} obtained from FE analysis. The contribution of heave to N_{vs} increases with pipe displacement for the range of $\tilde{v}$ simulated in this study. However, it is to be noted that downward movement of sand particles and infilling the cavity below the pipe could slow down the formation of heave and even reduce previously formed heave together with change in shape (trapezoid to triangular), especially when the pipe moves closer to the ground surface, as observed in physical experiments (Schupp et al. 2006; Wang et al. 2012). In other words, the contribution of heave decreases at large displacements, which is shown schematically by the dashed line (BC) in Fig. 8(c). These processes could not be simulated using the present numerical technique. Therefore, for structural response of the pipeline presented in the following sections, the post-peak segment of the force–displacement curve is defined by AB′C (Fig. 8(c)), where F_v at B′ is calculated using Eq. (4) without heave and it mobilizes at $v = v_s$.

Wang et al. (2012) showed that the post-peak segments of the uplift curves for loose sand for varying burial depths tend to follow a *backbone curve* similar to Eq. (4). There is only one post-peak segment in loose sand. However, an F_v–$\tilde{v}$ curve for dense sand has two post-peak segments—a quick reduction of F_v just after the peak, followed by the gradual reduction after $\tilde{v}_s$. Figure 8(a) shows that, for dense sand, the post-peak segments even after F_{vs}, do not lie on a unique line.

Effect of post-peak degradation of uplift resistance on upheaval buckling

Finite element analysis is performed to investigate the structural response of a steel pipeline having the following properties: outside diameter (D) of 298.5 mm, wall thickness (t) of 12.7 mm, concrete coating thickness (t_c) of 50 mm, steel yield strength (σ_y) of 448 MPa and steel thermal expansion coefficient (α) of 11×10^{-6} °C^{-1}. The pipe is buried in dense sand (D_r = 90%, γ' = 10 kN/m^3) at an embedment ratio ($\widetilde{H}$) of 3. The density of steel, concrete, seawater and oil in the pipe are 7850 kg/m^3, 2800 kg/m^3, 1025 kg/m^3 and 800 kg/m^3, respectively, which gives submerged pipe weight (oil-filled) of 1.6 kN/m.

To initiate upheaval buckling response, associated with increasing oil temperature (T), two initial imperfection ratios (v_0/L_0) of 0.005 (v_0 = 0.16 m, L_0 = 31.56 m) and 0.011 (v_0 = 0.45 m, L_0 = 41.05 m) are considered, where v_0 is the maximum initial vertical imperfection and L_0 is the initial imperfection length. The initial shape of the pipe is defined using Taylor and Tran (1996) empathetic model. A 3,500 m long pipe is simulated to avoid boundary effect in the buckled section. The modified Riks method is used to capture any snap-through buckling response that may occur (Dassault Systèmes 2010; Liu et al. 2014).

The force–displacement behaviour of soil is defined using three sets of nonlinear independent spring formulations that do not consider load coupling or interaction (e.g. Kenny and Jukes, 2015). For the modelling of upward resistance, two types of force–displacement relations are used. In Model-1, the F_v–v relation is defined as OAB′C as shown in Fig. 8(c). Using Eqs. (3) and (4), respectively, the uplift resistances at point A (9.14 kN/m) and B′ (5.16 kN/m) are calculated with v_p = 9.3 mm and v_s = 61.5 mm, as discussed above. The Model-II is same as the Model-I but without post-peak degradation where F_v remains constant after point A (i.e. elastic, perfectly plastic behaviour). Based on ALA (2005), the axial and vertical downward soil resistances of 4.62 kN/m and 607.5 kN/m, respectively, are calculated, which mobilize at 3 mm and 30 mm displacements, respectively.

Figure 9 shows the variation of temperature increase with the maximum buckle amplitude (v_m). For both v_0/L_0 ratios, T–v_m curve with post-peak reduction is below that without any reduction. Previous studies suggested a number of permissible temperature increase criteria including: (i) the critical (T_c) and safe (T_s) temperature for snap-through buckling response (represented by the circle and square symbols in Fig. 9), (ii) temperature required for the onset of first yield (T_y) for stable buckling (i.e. maximum stress = σ_y) (Hobbs et al. 1981; Taylor and Gan 1986). In this study, the maximum stress is calculated from axial stress and bending moment obtained from the numerical simulations. For the snap-through buckling response case (v_0/L_0 = 0.005), Fig. 9 shows the reduction of T_c and T_s of 10 °C and 23 °C, respectively, when the post-peak reduction in uplift resistance is considered. For the stable buckling case (v_0/L_0 = 0.011), the post-peak reduction could decrease T_y by 17 °C. Note that previous studies also recognized the importance of post-peak reduction of uplift resistance and suggested to use full force–displacement curve considering large vertical displacements (Klever et al. 1990; Goplen et al. 2005; Wang et al. 2009).

Conclusions

The uplift behaviour of buried pipeline in dense sand is investigated using finite element modelling. The stress–strain behaviour of soil is modeled using a modified Mohr–Coulomb (MMC) model, which considers the variation of angles of internal friction (ϕ') and dilation (ψ) with plastic shear strain, density and confining pressure, as observed in laboratory tests on dense sand. Comparison with a model test result shows that force–displacement, soil deformation and failure mechanisms can be explained from the variation of ϕ′ and ψ with loading. Simplified equations are proposed to establish the force–displacement curves for practical application. The following conclusions can be drawn from this study:

i. Slip planes do not reach the ground surface when the peak resistance is mobilized for higher burial depths.

ii. The proposed MMC model can simulate the rapid reduction of resistance after the peak, followed by gradual reduction at large displacement, as observed in model tests. However, the Mohr–Coulomb model shows a linear reduction of resistance due to change in cover depth.

iii. For an embedment ratio of 3–4, soil failure initiates with slip plane mechanisms and then the flow around mechanisms are observed at large displacement.

iv. The angle of inclination of the slip planes to the vertical (θ) is approximately equal to the peak dilation angle when the peak resistance mobilizes. However, it decreases with upward displacement due to decreases in the dilation angle. The angle θ significantly influences the weight of the soil wedge and thereby uplift resistance.

v. Uplift resistance at large displacement does not remain constant but decreases with upward displacement.

vi. Displacement required to complete initial softening increases significantly with the H/D ratio, as compared to the peak displacement.

vii. Post-peak reduction of uplift resistance could significantly reduce the permissible temperature during operation to avoid upheaval buckling.

Acknowledgements

The works presented in this paper have been supported by the Research and Development Corporation of Newfoundland and Labrador, Chevron Canada Limited and the Natural Sciences and Engineering Research Council of Canada (NSERC).

Notation

The following abbreviations and symbols are used in this paper:

TX = triaxial;

PS = plane strain;

PIV = particle image velocimetry;

LEM = limit equilibrium method;

MC = Mohr–Coulomb model;

MMC = Modified Mohr–Coulomb model;

A_ψ = slope of $(\phi'_p - \phi'_c)$ vs. I_R curve;

C_1, C_2 = material constants;

D_r = relative density;

D = pipe diameter;

E = Young's modulus;

FE = finite element;

F_v = uplift force;

F_{suc} = suction force under the pipe;

F_{vp} = peak uplift force;

F_{vs} = after softening uplift force;

$Fvp_{\_LEM}$ = F_{vp} calculated by LEM;

$Fvp_{\_FE}$ = F_{vp} calculated by FE;

H = distance from ground surface to the center of pipe;

$\widetilde{H}$ = embedment ratio (=H/D);

I_R = relative density index;

I_D = relative density/100;

K = material constant;

K_0 = at-rest earth pressure coefficient;

LEM = limit equilibrium method;

L_0 = initial imperfection length;

m = material constant;

N_v = normalized uplift force;

N_{vp} = normalized peak uplift force;

N_{vs} = value of N_v after softening;

Q, R = material constants (Bolton 1986);

UHB = upheaval buckling;

S_v = vertical component of shear resistance;

t_c = concrete coating thickness;

T_c = critical temperature;

T_s = safe temperature;

T_y = temperature required for onset of first yield;

W_s = submerged weight of lifted soil wedge;

k_ψ = slope of $(\phi'_p - \phi'_c)$ vs. ψ_p curve;

n = an exponent;

p' = mean effective stress;

p'_a = atmospheric pressure (=100 kPa);

v = vertical displacement of pipe;

v_0 = maximum initial vertical imperfection;

v_m = maximum buckle amplitude;

$\tilde{v}$ = normalized upward displacement of pipe (= v/D);

$\tilde{v}_p$ = $\tilde{v}$ required to mobilize N_{vp};

$\tilde{v}_s$ = $\tilde{v}$ required to mobilize N_{vs};

μ = friction coefficient between pipe and soil;

θ = inclination of slip plane to the vertical;

$\Delta\varepsilon_1^p$ = major principal plastic strain increment;

$\Delta\varepsilon_3^p$ = minor principal plastic strain increment;

$\dot{\epsilon}_{ij}^p$ = plastic deviatoric strain rate;

ϕ' = mobilized angle of internal friction;

ϕ'_{in} = ϕ' at the start of plastic deformation;

ϕ'_p = peak friction angle;

ϕ'_c = critical state friction angle;

ϕ_μ = pipe–soil interface friction angle;

ψ = mobilized dilation angle;

ψ_p = peak dilation angle;

ψ_p^R = representative value of the maximum dilation angle;

τ_f = shear resistance along the shear band;

γ = unit weight of soil;

γ^p = engineering plastic shear strain;

γ_p^p = γ^p required to mobilize ϕ'_p;

γ_c^p = strain-softening parameter; and

$\Delta\gamma^p$ = plastic strain increment.

References

Aiban, S. A., and Znidarčić, D. (1995). "Centrifuge modeling of bearing capacity of shallow foundations on sands." *J. of Geotech. Eng.*, 121(10), 704−712.

American Lifelines Alliance (ALA). (2005). "Guidelines for the design of buried steel pipe." <https://www.americanlifelinesalliance.com/pdf/Update061305.pdf > (Mar. 13, 2017).

American Petroleum Institute (API). (1987). "Recommended practice for planning, designing and constructing fixed offshore platforms." *API Recommended practice*, 2A (RP 2A), 17th Ed.

Aynbinder, A.B., and Kamershtein, A.G. (1982). "Raschet magistral'nykh truboprovodov na prochnost' i ustoichivost' [Calculation of trunk pipe for strength and stability]." Moscow (In Russian).

Bolton, M. D. (1986). "The strength and dilatancy of sands." *Géotechnique*, 36(1), 65−78.

Bransby, M. F., and Ireland, J. (2009). "Rate effects during pipeline upheaval buckling in sand." *Proc., ICE – Geotech. Eng.*, 162(5), 247−258.

Bransby, M.F., Newson, T. A. and Davies, M. C. R. (2002). "Physical modelling of the upheaval resistance of buried offshore pipelines." *Proc., Intl. conf. on physical modelling in geotechnics*, Kitakyushu, Japan.

Cathie D.N., Jaeck C., Ballard J-C and Wintgens J-F. (2005). "Pipeline geotechnics – state-of-the-art." *Proc., Int. Symp. on Frontiers in Offshore Geotechnics*, Taylor & Francis, 95−114.

Chakraborty, D. and Kumar, J. (2014). "Vertical uplift resistance of pipes buried in sand." *J. of Pipe. Sys. Eng. and Prac.*, 5(1).

Chakraborty, T., and Salgado, R. (2010). "Dilatancy and shear strength of sand at low confining pressures." *J. Geotech. Geoenv. Eng.*, 136(3), 527−532.

Cheuk, C. Y., White, D. J. and Bolton, M. D. (2005). "Deformation mechanisms during the uplift of buried pipelines in sand." *Proc., 16th Intl. Conf. on Soil Mech.s and Geotech. Eng.*, Osaka, 1685–1688.

Cheuk, C. Y., White, D. J., and Bolton, M. D. (2008). "Uplift mechanisms of pipes buried in sand." *J. Geotech. Geoenv. Eng.*, 134(2), 154–163.

Chin, E. L., Craig, W. H., and Cruickshank, M. (2006). "Uplift resistance of pipelines buried in cohesionless soil." *Proc., 6th Int. Conf. on Physical Modelling in Geotechnics*, Ng, Zhang, and Wang, eds., Vol. 1, Taylor & Francis Group, London, 723–728.

Clukey, E.C., Jackson, C.R., Vermersch, J.A., Koch, S.P., and Lamb, W.C. (1989). "Natural densification by wave action of sand surrounding a buried offshore pipeline." *Proc., Offshore technology conference*, Houston, Texas.

Dassault Systèmes. (2010). *ABAQUS* [computer prog.]. Dassault Systèmes, Inc., Providence, R.I.

Det Norske Veritas (DNV). (2007). "Global buckling of submarine pipelines—Structural design due to high temperature/high pressure." *DNV-RP-F110*, Det Norske Veritas, Baerum, Norway.

Dickin, E.A. (1994). "Uplift resistance of buried pipelines in sand." *Soils and Found.*, 34(2), 41–48.

Dutta, S., Hawlader, B. & Phillips, R. (2015). "Finite element modeling of partially embedded pipelines in clay seabed using Coupled Eulerian–Lagrangian method." *Can. Geot. J.*, 52(1), 58–72.

Eiksund, G., Langø, H., Øiseth, E. (2013). "Full-scale test of uplift resistance of trenched pipes." *Int. J. of Offshore and Polar Eng.*, 23(4), 298–306.

Farhadi, B. and Wong, R. C. K. (2014). "Numerical modeling of pipe-soil interaction under transverse direction." *Proc., Int. Pipe. Conf.*, Calgary, Canada. IPC 2014-33364.

Goplen, S., Strom, P, Levold, E., and Mork, J. (2005). "Hotpipe jip: HP/HT buried pipelines." *Proc., 24th International Conference on Ocean, Offshore and Arctic Engineering (OMAE 2005)*, Halkidiki, Greece.

Hobbs, R. E. (1984). "In-service buckling of heated pipelines." *J. of Trans. Eng.*, ASCE, 110(2), 175–189.

Huang, B., Liu, J., Ling, D. and Zhou, Y. (2015). "Application of particle image velocimetry (PIV) in the study of uplift mechanisms of pipe buried in medium dense sand." *J Civil Struct. Health Monit.*, 5(5), 599–614.

Kenny, S. and Jukes, P. (2015). "Pipeline/soil interaction modelling in support of pipeline engineering design and integrity." Oil and Gas Pipelines: Integrity and Safety Handbook, R.W. Revie Editor, ISBN 978-1-118-21671-2, John Wiley & Sons Ltd., 93p.

Klever, F. J., Van Helvoirt, L. C., and Sluyterman, A. C. (1990). "A dedicated finite-element model for analyzing upheaval bucking response of submarine pipelines." *Proc., 22nd Annual Offshore Technology Conf.*, Houston, 529–538.

Jung, J.K., O'Rourke, T.D., and Olson, N.A. (2013). "Uplift soil–pipe interaction in granular soil." *Can. Geotech. J.*, 50(7), 744–753.

Lings, M. L., and Dietz, M. S. (2004). "An improved direct shear apparatus for sand." *Géotechnique*, 54(4), 245−256.

Liu, R., Xiong, H., Wu, X.L., Yan, S.W. (2014). "Numerical studies on global buckling of subsea pipelines." *Ocean Eng*. 78, 62–72

Loukidis D and Salgado R. (2011). "Effect of relative density and stress level on the bearing capacity of footings on sand." *Géotechnique*, 61(2), 107–19.

Merifield, R. S., Sloan, S. W., Abbo, A. J. and Yu, H. S. (2001). "The ultimate pullout capacity of anchors in frictional soils." *Proc., 10th Int. Conf. on Computer Methods and Advances in Geomechanics*, Tucson, AZ, 1187–1192.

Palmer, A.C., White, D.J., Baumgard, A.J., Bolton, M.D., Barefoot, A.J., Finch, M., Powell, T., Faranski, A.S., and Baldry, J.A.S. (2003). "Uplift resistance of buried submarine pipelines: comparison between centrifuge modelling and full-scale tests." *Géotechnique*, 53(10), 877−883.

Pike, K. (2016). "Physical and numerical modelling of pipe/soil interaction events for large deformation geohazards." PhD thesis, Memorial University of Newfoundland, St. John's, Canada.

Pike, K., and Kenny, S. (2016). "Offshore pipelines and ice gouge geohazards: Comparative performance assessment of decoupled structural and coupled continuum models." *Can. Geotech. J.*, 53(11), 1866−1881.

Randolph, M.F., Jamiolkowski, M.B. and Zdravkovic, L. (2004). "Load carrying capacity of foundations." *Proc. Skempton Memorial Conf.*, London 1, 207–240.

Roy, K., Hawlader, B.C., Kenny, S. and Moore, I. (2016). "Finite element modeling of lateral pipeline−soil interactions in dense sand." *Can. Geotech. J.*, 53(3), 490−504.

Roy, K. (2017). "Numerical modeling of pipe−soil and anchor−soil interactions in dense sand." PhD thesis, Memorial University of Newfoundland, St. John's, NL, Canada.

Roy, K., Hawlader, B.C., Kenny, S. and Moore, I. (2018). "Uplift failure mechanisms of pipes buried in dense sand." *ASCE Int. J. Geomech.* (In press).

Saboya, F.A. Jr., Santiago, P. A.C., Martins, R.R., Tibana, S., Ramires, R.S. and Araruna, J. T. Jr. (2012). "Centrifuge test to evaluate the geotechnical performance of anchored buried pipelines in sand." *J. of Pipe. Sys. Eng. and Prac.*, 3(3).

Schaminée, P., Zorn, N., and Schotman, G. (1990). "Soil response for pipeline upheaval buckling analyses: Full-scale laboratory tests and modelling." *Proc., Off. Technol. Conf.*, Houston, 563–572.

Schupp, J., Byrne, B. W., Eacott, N., Martin, C. M., Oliphant, J., Maconochie,A., and Cathie, D. (2006). "Pipeline unburial behaviour inloose sand." *Proc., 25th Int. Conf. on Offshore Mechanics and Arctic Engineering*, Hamburg, Germany, OMAE2006-92541.

Stone, K. J. L., and Newson, T. A. (2006). "Uplift resistance of buried pipelines: An investigation of scale effects in model tests." *Proc., 6th Int. Conf. on Physical Modelling in Geotechnics*, Ng, Zhang, and Wang, eds., Vol. 1, Taylor & Francis Group, London, 741–746.Tatsuoka, F., Okahara, M., Tanaka, T., Tani, K., Morimoto, T., and Siddiquee, M. S. A. (1991). "Progressive failure and particle size effect in bearing capacity of a footing on sand." *Geotech. Spec. Publ.*, 27(2), 788–802.

Taylor, N. and Gan, A.B. (1986). "Submarine Pipeline Buckling-Imperfection Studies." *Thin-Walled Structures*, 4(4), 295–323.

Thusyanthan, N. I., Mesmar, S., Wang, J. and Haigh, S. K. (2010). "Uplift resistance of buried pipelines and DNV-RP-F110." *Proc., Off. Pipeline and Tech. Conf.*, Amsterdam, 24–25.

Trautmann, C. (1983). "Behavior of pipe in dry sand under lateral and uplift loading." PhD thesis, Cornell University, Ithaca, NY.

Wang, J., Eltaher, A., Jukes, P., Sun, J., and Wang, F. S. (2009). "Latest Developments in Upheaval Buckling Analysis for Buried Pipelines." *Proc., Int. Offshore and Polar Engineering Conf.*, The International Society of Offshore and Polar Engineers (ISOPE), California, 594–602.

Wang, J., Ahmed, R., Haigh, S. K., Thusyanthan, N. I., and Mesmar, S. (2010). "Uplift resistance of buried pipelines at low cover–diameter ratios." *Proc., Off. Technol. Conf., OTC-2010-20912*.

Wang, J., Haigh, S. K., Forrest, G. and Thusyanthan, N. I. (2012). "Mobilization distance for upheaval buckling of shallowly buried pipelines." *J. Pipe. Syst. Eng. Prac.*, 3(4), 106–114.

White, D. J., Barefoot, A. J. & Bolton, M. D. (2001). "Centrifuge modelling of upheaval buckling in sand." *Int. J. Phys. Modelling Geomech*., 2, 19–28.

White, D. J., Take, W. A., and Bolton, M. D. (2003). "Soil deformation measurement using particle image velocimetry (PIV) and photogrammetry." *Geotechnique*, 53(7), 619–631.

White, D.J., Cheuk, C.Y, and Bolton, M.D. (2008). "The Uplift resistance of pipes and plate anchors buried in sand." *Géotechnique*, 58(10), 771–779.

Yimsiri, S., Soga, K., Yoshizaki, K., Dasari, G., and O'Rourke, T. (2004). "Lateral and upward soil–pipeline interactions in sand for deep embedment conditions." *J. Geotech. Geoenv. Eng.*, 130(8), 830−842.

Table 1: Equations for Modified Mohr–Coulomb Model (MMC) (summarized from Roy et al. 2016)

Description	Constitutive Equations
Relative density index	$I_R = I_D(Q - \ln p') - R$ where $I_D = D_r(\%)/100$ & $0 \le I_R \le 4$
Peak friction angle	$\phi'_p - \phi'_c = A_\psi I_R$
Peak dilation angle	$\psi_p = \dfrac{\phi'_p - \phi'_c}{k_\psi}$
Strain-softening parameter	$\gamma_c^p = C_1 - C_2 I_D$
Plastic shear strain at ϕ'_p and ψ_p	$\gamma_p^p = \gamma_c^p \left(\dfrac{p'}{p'_a}\right)^m$
Mobilized friction angle in Zone-II	$\phi' = \phi'_{in} + \sin^{-1}\left[\left(\dfrac{2\sqrt{\gamma^p \gamma_p^p}}{\gamma^p + \gamma_p^p}\right)\sin(\phi'_p - \phi'_{in})\right]$
Mobilized dilation angle in Zone-II	$\psi = \sin^{-1}\left[\left(\dfrac{2\sqrt{\gamma^p \gamma_p^p}}{\gamma^p + \gamma_p^p}\right)\sin(\psi_p)\right]$
Mobilized friction angle in Zone-III	$\phi' = \phi'_c + \left(\phi'_p - \phi'_c\right)\exp\left[-\left(\dfrac{\gamma^p - \gamma_p^p}{\gamma_c^p}\right)^2\right]$
Mobilized dilation angle in Zone–III	$\psi = \psi_p \exp\left[-\left(\dfrac{\gamma^p - \gamma_p^p}{\gamma_c^p}\right)^2\right]$
Young's modulus	$E = K p'_a \left(\dfrac{p'}{p'_a}\right)^n$

Note: Zone-I, -II and -III represent the elastic, pre-peak hardening, and post-peak softening of the stress–strain curve, respectively (see Fig. 1(b)).

Table 2: Geometry and soil parameters used in the FE analyses

Parameter	Model test (Parametric study)
External diameter of pipe, D (mm)	100 (300, 500)
K	150
n	0.5
ν_{soil}	0.2
A_{ψ}	5
k_{ψ}	0.8
ϕ'_{in} (°)	29
C_1	0.22
C_2	0.11
m	0.25
Critical state friction angle, ϕ'_c (°)	35
Relative density, D_r (%)	92
Unit weight, γ (kN/m^3)	16.87
Interface friction coefficient, μ	0.32
Depth of pipe, $\widetilde{H}$	3 (1, 1.5, 2.0, 2.5, 3.5, 4.0)

Note: Numbers in parenthesis in right column show the values used for parametric study

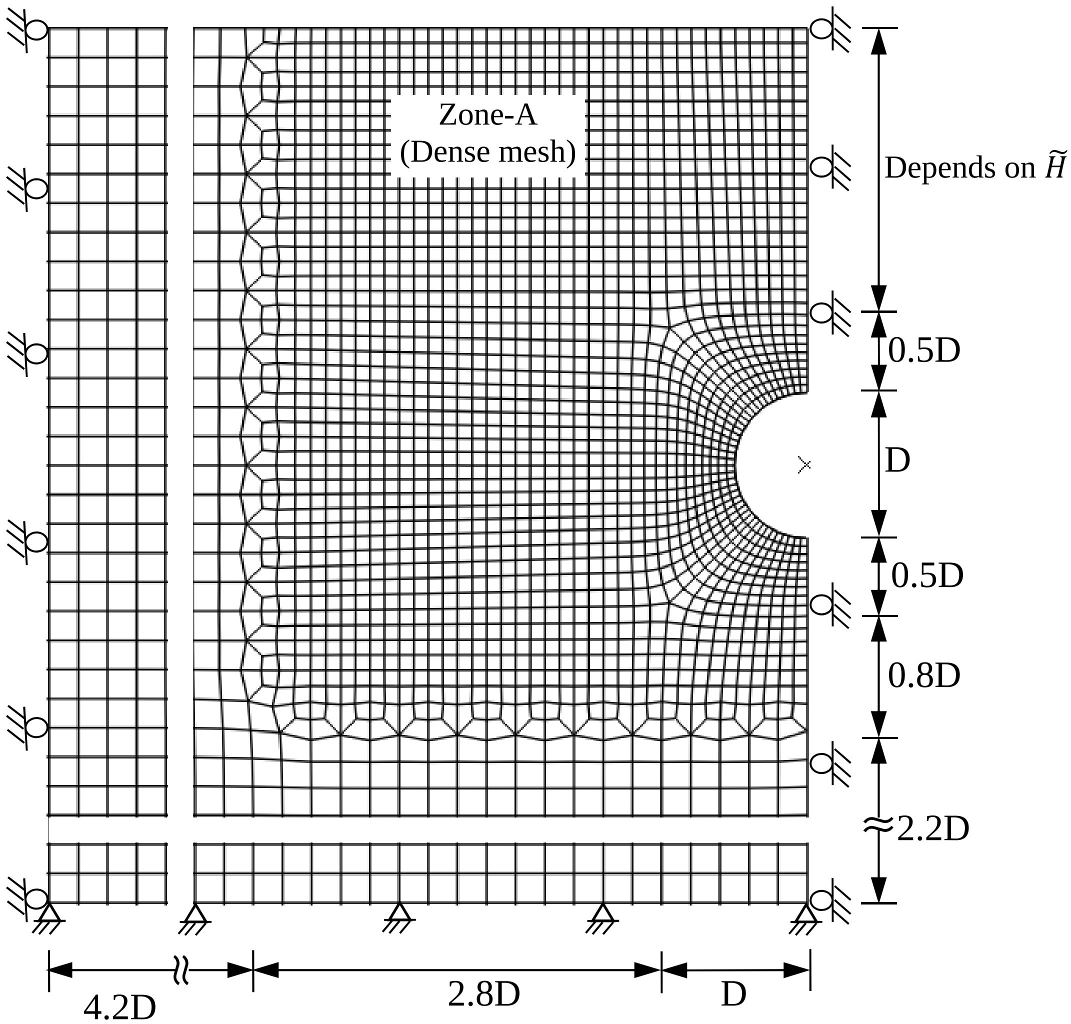

(a)

Figure 1: Finite element modelling: (a) finite element mesh; (b) mobilized friction and dilation angles

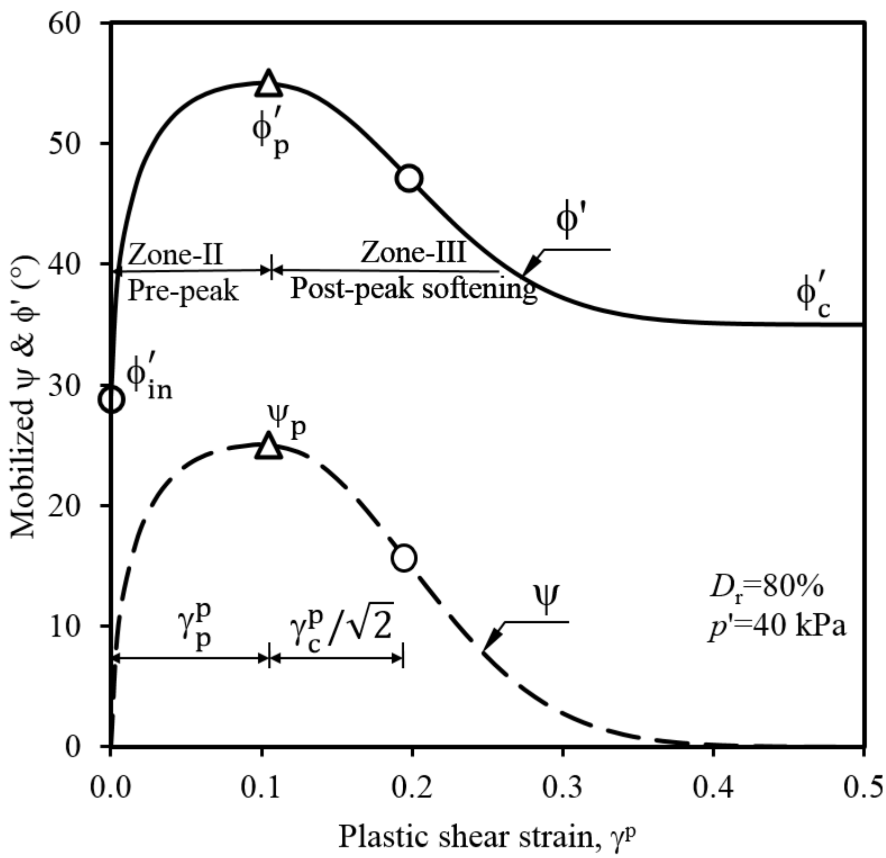

(b)

Figure 1: Finite element modelling: (a) finite element mesh; (b) mobilized friction and dilation angles

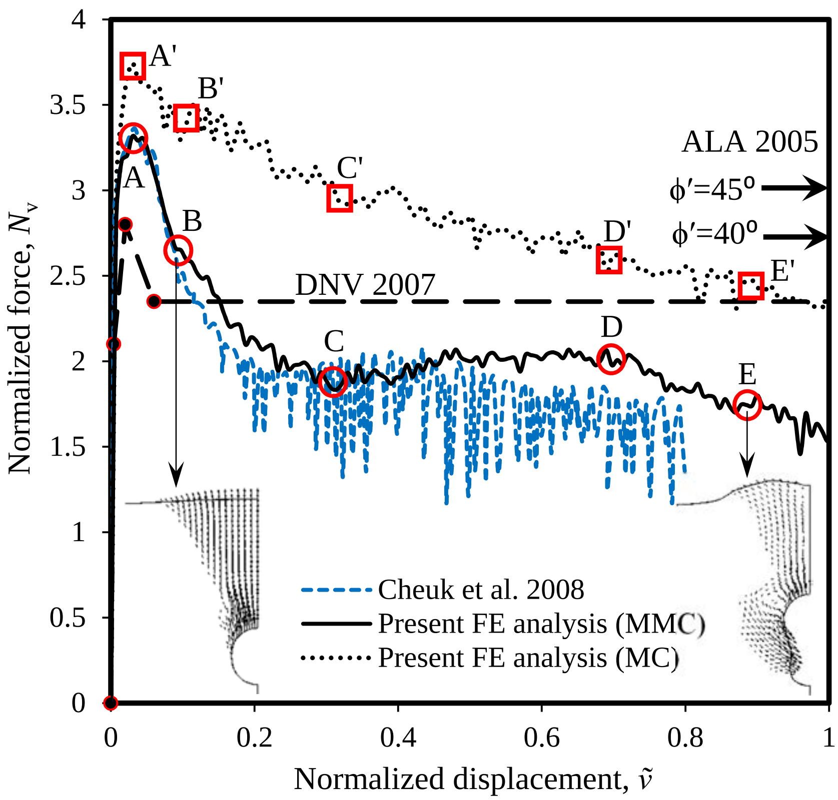

Figure 2: Comparison between FE simulation and model test results

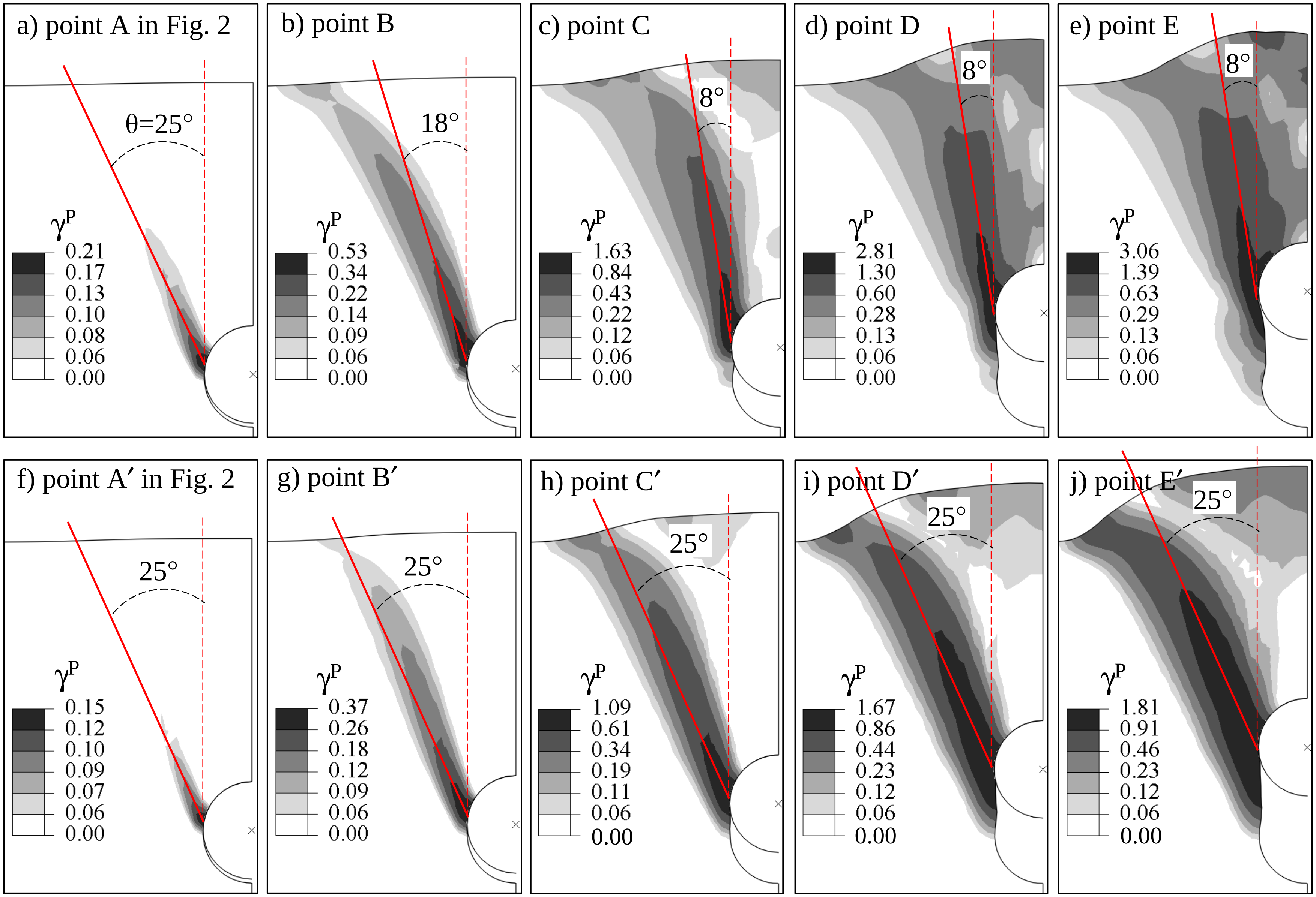

Figure 3: Shear band formation: a–e for modified Mohr–Coulomb model and f–j for Mohr–Coulomb model

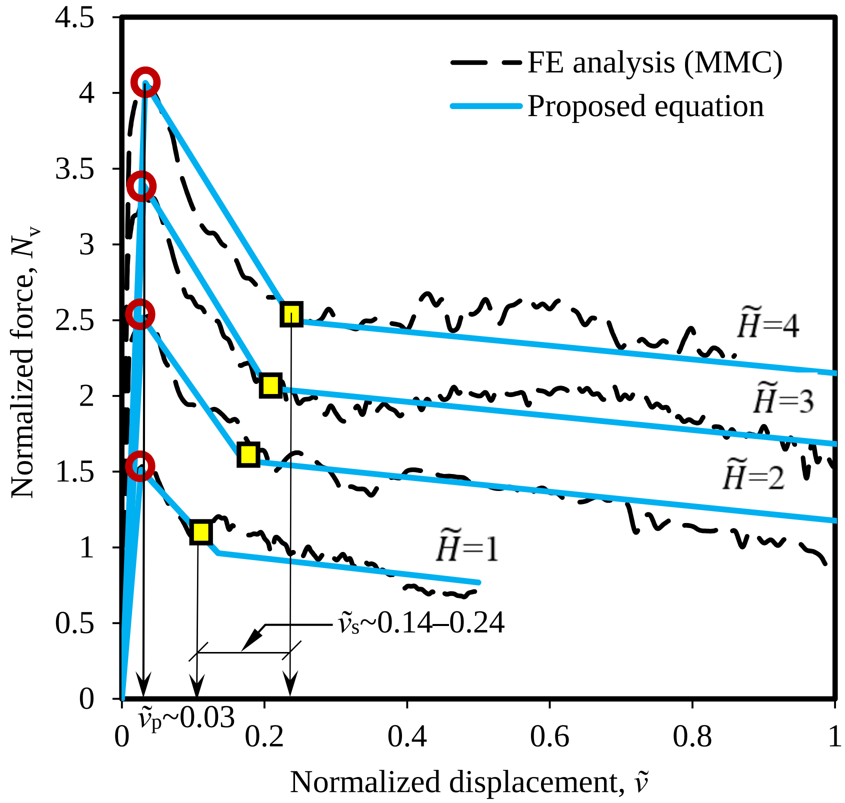

Figure 4: Comparison between simplified equations and FE results for different $\widetilde{H}$

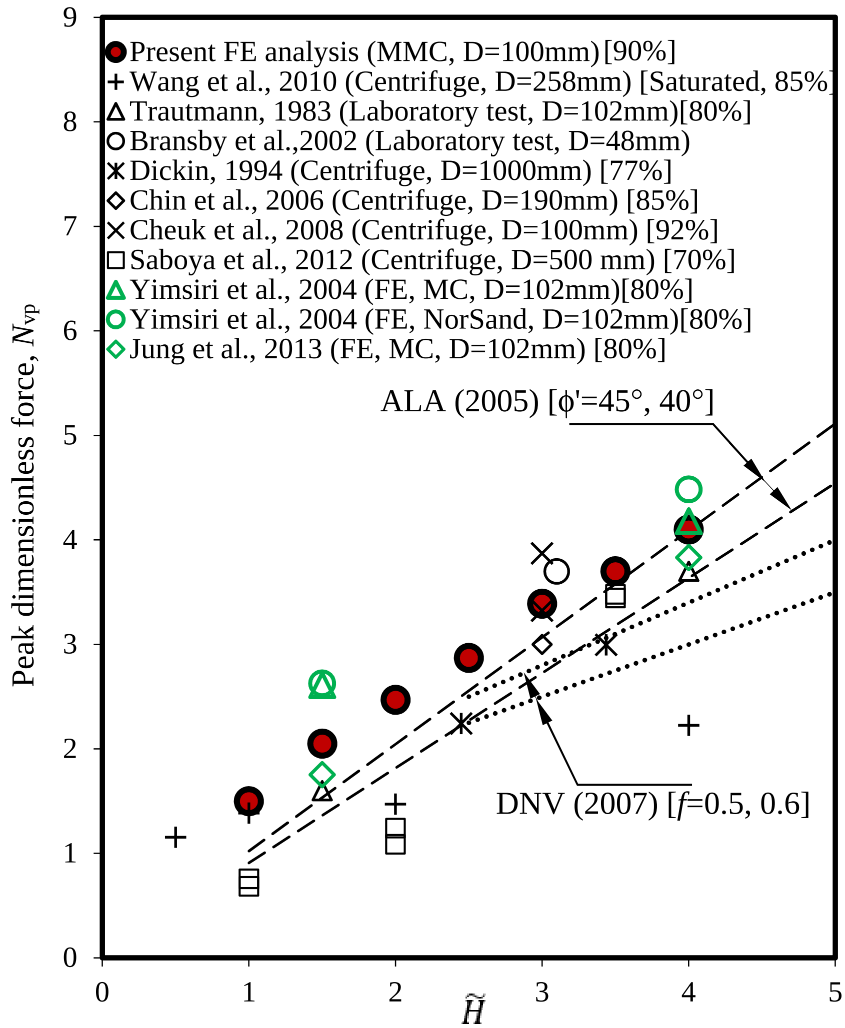

Figure 5: Comparison of peak uplift force from numerical analysis and physical model tests

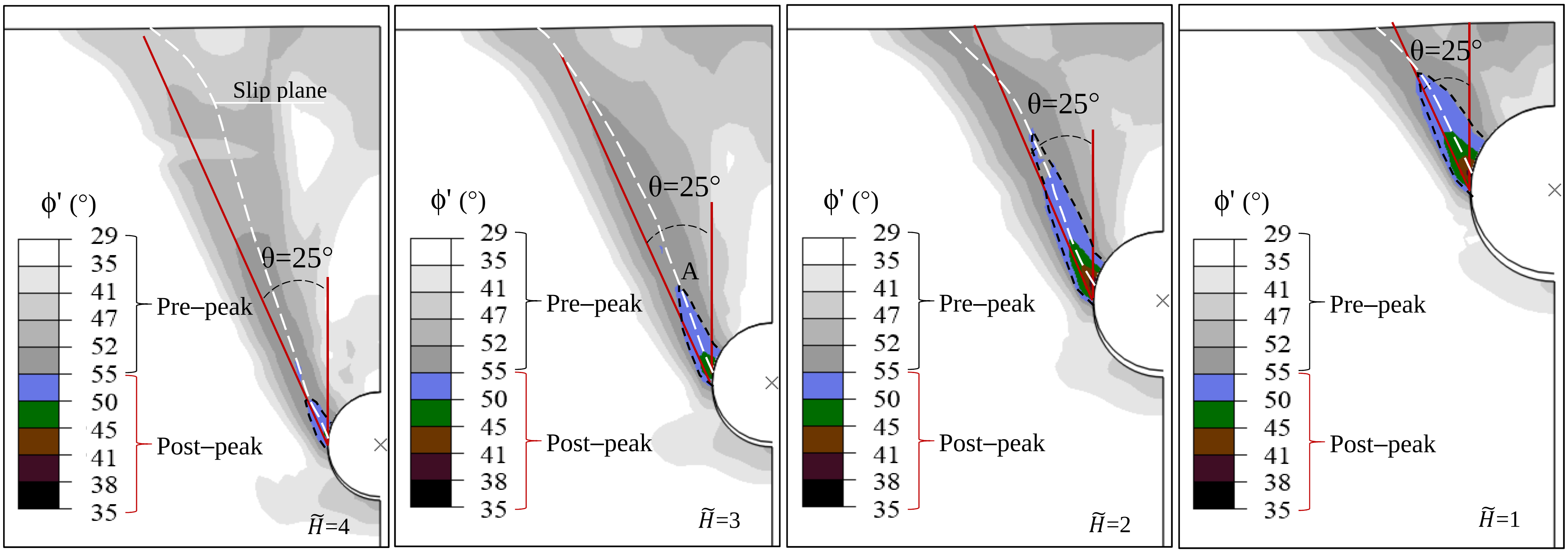

Figure 6: Effect of burial depth on peak resistance: (a) soil failure

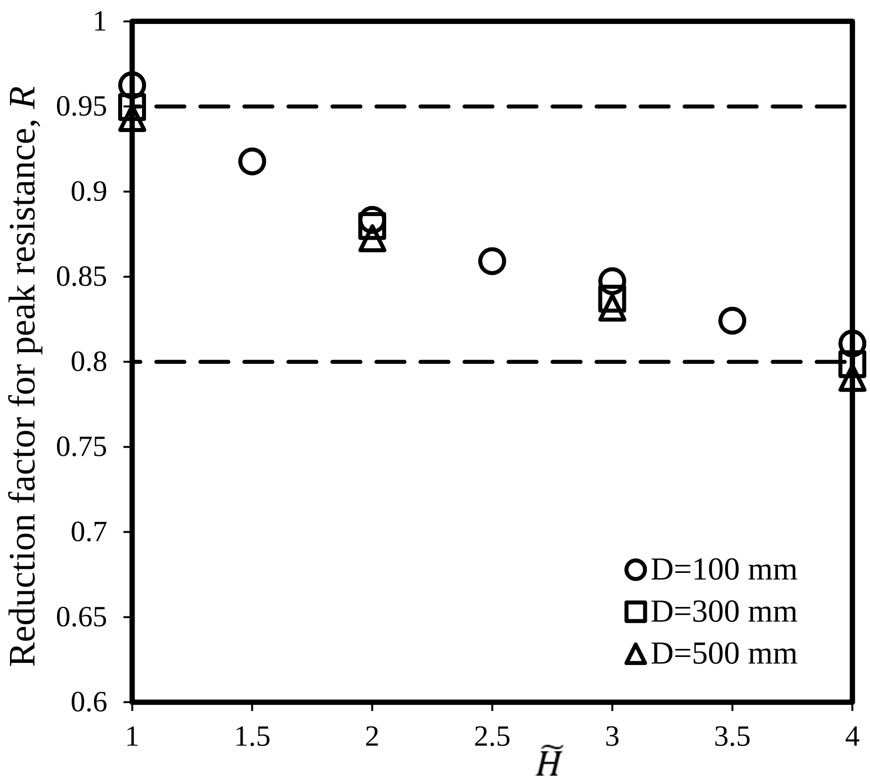

Figure 6: Effect of burial depth on peak resistance: (b) reduction factor, *R*

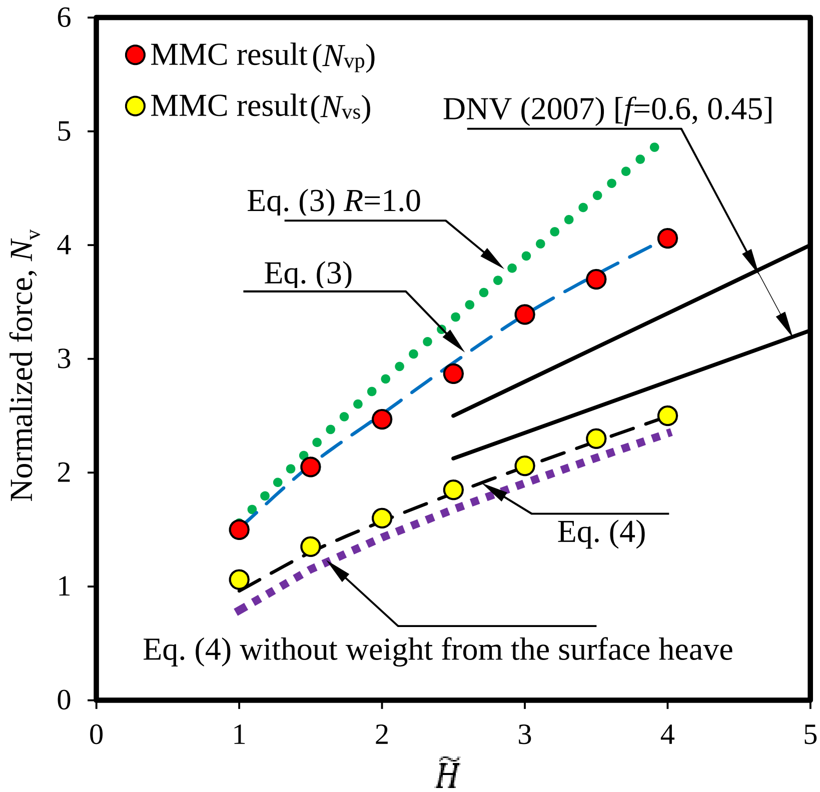

Figure 7: Performance of simplified equations: (a) comparison with FE analysis

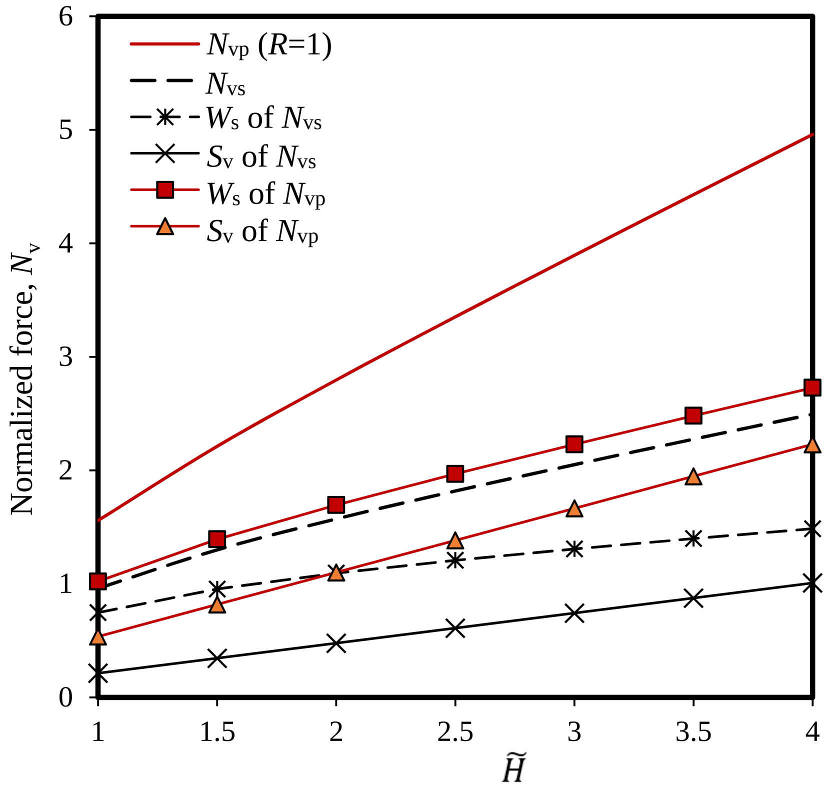

Figure 7: Performance of simplified equations: (b) contribution of weight and shear components

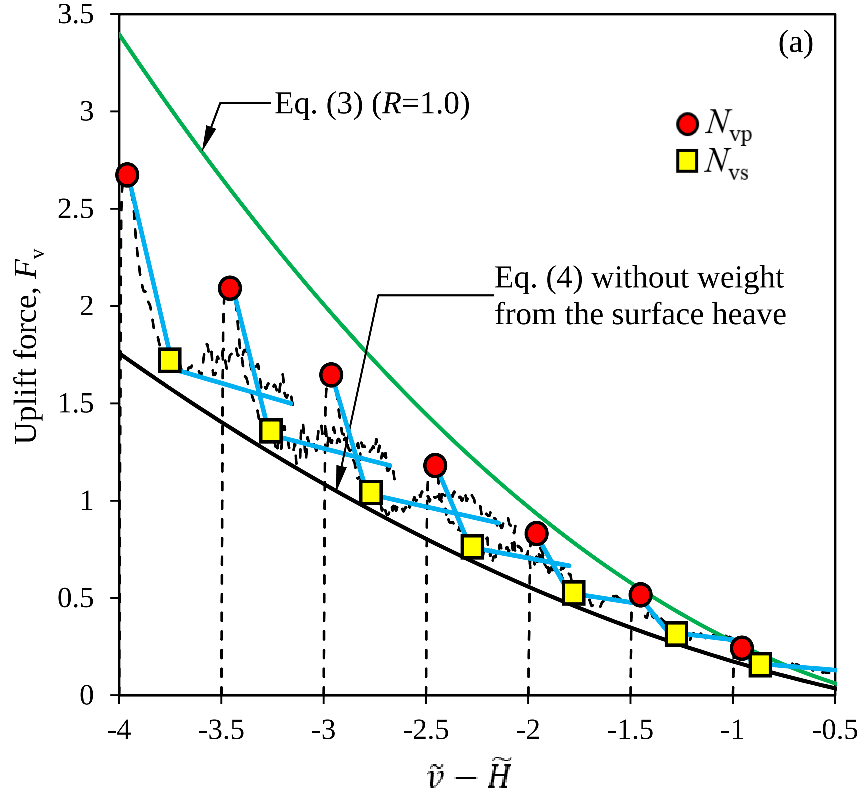

Figure 8: Comparison between force–displacement curves from FE analyses and simplified equations: (a) F_v vs $\tilde{v} - \tilde{H}$ plots (b) Idealized heave, and (c) Idealized $F_v - v$ curve

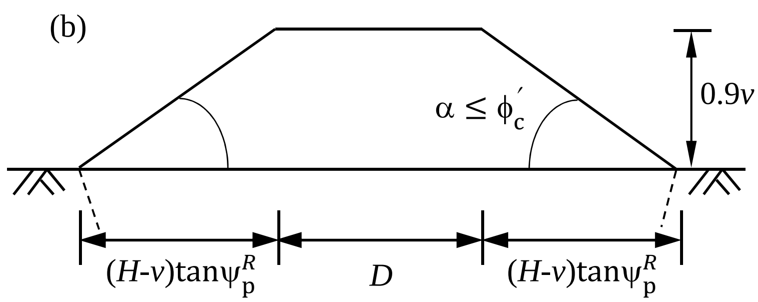

Figure 8: Comparison between force–displacement curves from FE analyses and simplified equations: (a) F_v vs $\tilde{v} - \tilde{H}$ plots (b) Idealized heave, and (c) Idealized $F_v - v$ curve

(c)

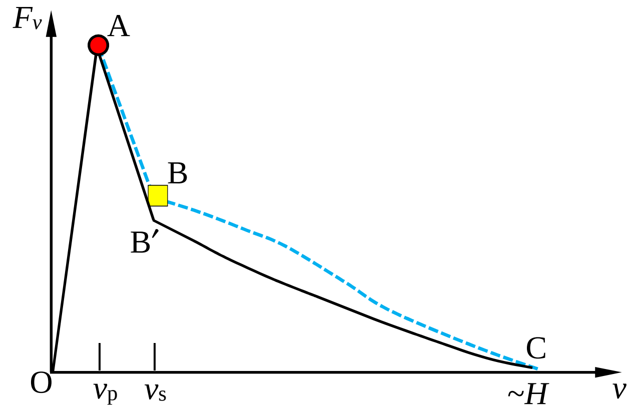

Figure 8: Comparison between force–displacement curves from FE analyses and simplified equations: (a) F_v vs $\tilde{v} - \tilde{H}$ plots (b) Idealized heave, and (c) Idealized $F_v - v$ curve

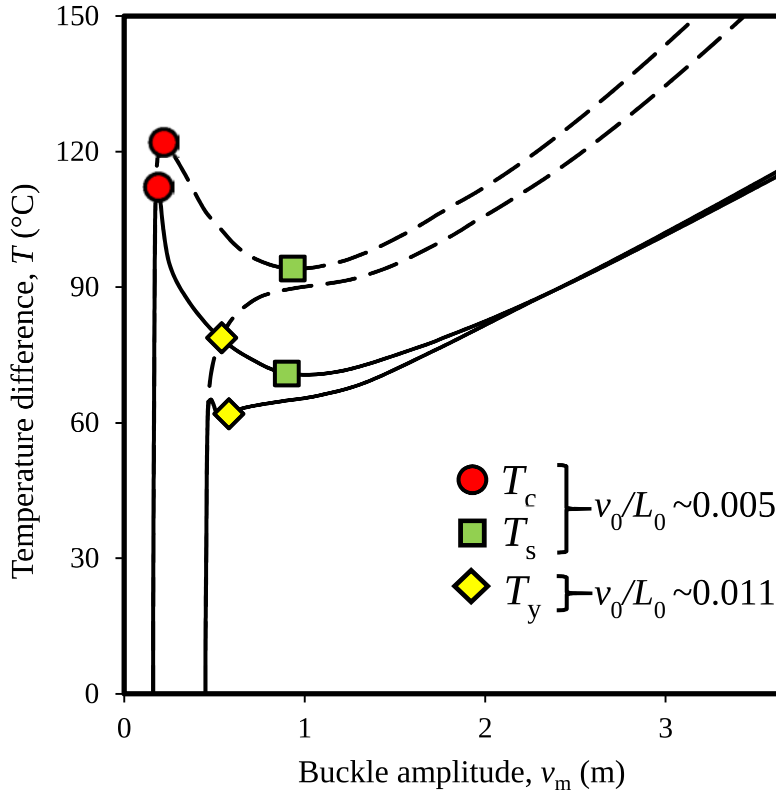

Figure 9: Effect of post-peak reduction of uplift resistance on permissible temperatures